Icarus 288 (2017) 53–68

Contents lists available at ScienceDirect

Icarus

journal homepage: www.elsevier.com/locate/icarus

Thrust fault modeling and Late-Noachian lithospheric structure of the circum-Hellas region, Mars

Isabel Egea-Gonzalez[a,b,*], Alberto Jiménez-Díaz[c], Laura M. Parro[c], Valle López[d], Jean-Pierre Williams[e], Javier Ruiz[c]

[a] Departamento de Física Aplicada, Universidad Politécnica de Cartagena, C/ Dr. Fleming s/n, Cartagena 30202, Spain
[b] Departamento de Física Aplicada. Escuela Politécnica Superior de Algeciras, Universidad de Cádiz, Algeciras, Cádiz 11202, Spain
[c] Departamento de Geodinámica, Facultad de Ciencias Geológicas, Universidad Complutense de Madrid, Madrid 28040, Spain
[d] Instituto de Geociencias, IGEO (CSIC, UCM), Madrid 28040, Spain
[e] Department of Earth and Space Sciences, University of California, Los Angeles, CA 90095, USA

ARTICLE INFO

Article history:
Received 22 July 2016
Revised 13 January 2017
Accepted 26 January 2017
Available online 29 January 2017

Keywords:
Mars
Mars, Interior
Tectonics
Thermal histories

ABSTRACT

The circum-Hellas area of Mars borders Hellas Planitia, a giant impact ~4.0–4.2 Ga old making the deepest and broadest depression on Mars, and is characterized by a complex pattern of fracture sets, lobate scarps, grabens, and volcanic plains. The numerous lobate scarps in the circum-Hellas region mainly formed in the Late Noachian and, except Amenthes Rupes, have been scarcely studied. In this work, we study the mechanical behavior and thermal structure of the crust in the circum-Hellas region at the time of lobate scarp formation, through the modeling of the depth of faulting beneath several prominent lobate scarps. We obtain faulting depths between ~13 and 38 km, depending on the lobate scarp and accounting for uncertainty. These results indicate low surface and mantle heat flows in Noachian to Early Hesperian times, in agreement with heat flow estimates derived from lithospheric strength for several regions of similar age on Mars. Also, faulting depth and associate heat flows are not dependent of the local crustal thickness, which supports a stratified crust in the circum-Hellas region, with heat-producing elements concentrated in an upper layer that is thinner than the whole crust.

1. Introduction

Lobate scarps are relatively common tectonic structures on the surface of the Moon, Mars and Mercury. These structures are linear or arcuate features that have asymmetric cross-sectional profiles, with a very steep scarp face and a more moderately sloped back scarp, and can exceed 1 km in elevation and several hundred kilometers in length (e.g., Watters and Robinson, 1999; Watters and Schultz, 2010). Lobate scarps offset the walls and floors of cross-cut craters suggesting they are expression of thrust faults which likely deform the crust down to the brittle-ductile transition depth (e.g., Schultz and Watters, 2001; Watters et al., 2002; Watters and Schultz, 2010). The brittle-ductile transition relates the mechanical structure of the lithosphere to the thermal structure. Therefore knowledge of the depth reached by a lobate scarp-related fault provides a means of estimating surface heat flows and subsurface temperatures at the time of faulting (e.g., Grott et al., 2007; Ruiz et al., 2008, 2009; Mueller et al., 2014).

In this work we focus on lobate scarp features in the circum-Hellas area of Mars. Hellas Planitia is a giant impact basin formed during the Early Noachian (Leonard and Tanaka, 2001), around 4.0–4.2 Ga (Frey, 2006; Fasset and Head, 2011), which forms the deepest and broadest depression on Mars, 9 km relief and 2000 km across (Smith et al., 1999). A complex region of fracture sets, lobate scarps, channels, grabens, and volcanic plains with a basin-controlled origin is established around Hellas. Some of these structures may be the surface expression of internal events triggered by the basin-forming impact (e.g., Bratt et al., 1985; Chicarro et al., 1985; Freed et al., 2001; Öhman et al., 2005).

Lobate scarps are numerous in the vicinity of Hellas (e.g., Wichman and Schultz, 1989). They mainly formed in the Late Noachian (see Tanaka et al., 2014), probably related to the crustal thickening and lateral pressure variations following the formation of the basin. These circum-Hellas lobate scarps include Amenthes Rupes, the largest lobate scarp on Mars, which is located between the Isidis and Hellas regions and is the more prominent member of a local thrust fault population (Watters and Robinson, 1999).

* Corresponding author:.
E-mail address: isabel.egea@uca.es (I. Egea-Gonzalez).

http://dx.doi.org/10.1016/j.icarus.2017.01.028
0019-1035/

Apart from several works focused on Amenthes Rupes, lobate scarps around Hellas have been scarcely studied. Schultz and Watters (2001) calculated the depth of the fault beneath Amenthes Rupes by modeling the topography across the lobate scarp through the elastic dislocation program Coulomb (Toda et al., 2005; Lin and Stein, 2004); those authors obtained best-fitting topography models from depths of faulting of 25–30 km. Grott et al. (2007) also followed a dislocation method for Amenthes Rupes, obtaining a depth of faulting of 32–40 km. Ruiz et al. (2008) analyzed the depth of the fault associated with Amenthes Rupes by using elastic modeling of a topographic profile perpendicular to the lobate scarp trace; they concluded that models that best match the topography above Amenthes Rupes were provided by a rectangular fault geometry with a depth of faulting that ranges between 27 and 35 km. Recently, Mueller et al. (2014) applied the fault-related fold theory to study the geometry of the fault associated with Amenthes Rupes, suggesting the presence of a listric fault that reaches a depth of 33–48 km. Finally, Grott et al. (2007) also studied the geometry of the thrust faults associated with two lobate scarps located in the Thaumasia highlands, obtaining faulting depths of 27–35 and 21–28 km, values similar to those found for Amenthes Rupes through dislocation methods for different authors.

Because thrust faults associated with the lobate scarps are considered to penetrate down to the brittle-ductile transition (BDT), which is temperature-controlled for a given composition, the above summarized faulting depth results can be used to model the thermal structure of the lithosphere, and hence used to derive the surface heat flow at the time of faulting. Thus, Ruiz et al. (2008, 2011) obtained a surface heat flow between 18 and 37 mW m^{-2} when Amenthes Rupes was formed. Similarly, Mueller et al. (2014) obtained a range of 24–33 mW m^{-2} for this lobate scarp based on their somewhat deeper BDT depth.

The effective elastic thickness of the lithosphere (T_e) is another way to characterize lithospheric mechanical behavior, used in other works analyzing the circum-Hellas region (e.g., McGovern et al., 2004). T_e is related to the total strength of the lithosphere including contributions from brittle and ductile layers and from elastic cores of the lithosphere (for a review see Watts, 2001). As mantle rock strength depends on temperature, the effective elastic thickness is greatly affected by the thermal state of the lithosphere.

Several effective elastic thickness estimates for Late Noachian and Early Hesperian times are available for the circum-Hellas area. Effective elastic thicknesses for Hellas South rim and Hellas West rim were calculated using gravity/topography admittance spectra in McGovern et al. (2004); these authors obtained T_e values of 20–120 km for Hellas south rim and an upper limit of 20 km for Hellas west rim. Ruiz et al. (2008) calculated a range for T_e of 19–35 km in the Amenthes region by means of a coherence analysis of topography and gravity spectra. T_e values for Hellas west rim and Amenthes region are similar to those found for other martian regions of similar age (for a review see Ruiz, 2014), but the upper part of the range for Hellas south rim may be considered high for Late Noachian/Early Hesperian times.

As T_e is also influenced by temperature, variations of this parameter may reflect differences in the local lithospheric thermal regime, and thus, T_e values can be used to estimate the surface heat flow. As effective elastic thickness values for Late Noachian and Early Hesperian times are available in the circum-Hellas region (McGovern et al., 2004; Ruiz et al., 2008), heat flows in the period of lobate scarps formation can also be analyzed by applying this method. Following this procedure McGovern et al. (2004) obtained heat flows of 20–40 and >30 mW m^{-2}, respectively, for the Hellas south and west rims. More refined calculations by Ruiz et al. (2011) for the same regions and T_e values yielded values of 12–40 mW m^{-2} and >21 mW m^{-2}, respectively, for the Hellas south and west rims. Similarly, for the Amenthes Rupes region Ruiz et al. (2008) calculated a heat flow of 31–49 mW m^{-2} from their range of T_e. These results overlap with those obtained by Ruiz et al. (2008, 2011) and (in a narrow range) by Mueller et al. (2014) from the BDT depth below Amenthes Rupes. Moreover, the heat flows deduced in the circum-Hellas regions are similar to those for other regions of similar age on Mars (Ruiz et al., 2011; Ruiz, 2014).

In this work, we study the mechanical and thermal structure of the lithosphere in the circum-Hellas region of Mars through the modeling of the depth of faulting beneath several prominent lobate scarps distributed throughout this region and bordering the Hellas basin (see Fig. 1). Then, we convert the obtained faulting depths, assumed as representative of the BDT, to heat flows. Next, with the help of a crustal thickness model for this region, we estimated crustal (radioactively generated) and subcrustal (mantle) heat flow components. Finally, we analyze and discuss the implications of our results for the structure of the crust in the circum-Hellas region and for the thermal state and evolution of Mars in Noachian to Early Hesperian times.

2. Selected lobate scarps

We have analyzed eight lobate scarps distributed around Hellas (Fig. 1; Table 1). Four of these structures are previously recognized and named lobate scarps: Pityusa Rupes, Chalcoporos Rupes, Thyles Rupes and Amenthes Rupes, which were classified as compressional structures by Tanaka et al. (2014). The rest of lobate scarps have been selected according to their geological and cross-cutting relationships that indicate they are contractional structures. Most of the selected lobate scarps are located on the ejecta blanket of Hellas, concentric to Hellas basin, constituting a “ring” between 2500 and 5000 km from the center of the basin. Lobate Scarp 7, which is closest (1200 km) to the basin center is the exception, with a distinct radial orientation. Scarcity of lobate scarps in the regions northeast and southwest of Hellas basin is probably related to the emplacement of volcanic materials in Malea Planum and Hesperia Planum, which are, respectively, of Noachian and Hesperian age (Tanaka et al., 2014). Fig. 2 shows the studied lobate scarps together with the locations of the topographic profiles that have been used in the modeling process.

Pityusa Rupes (numbered as 1 in Fig. 1 and Table 1) is a SE-NW-trending structure (Fig. 2a), about 150 km long and 600 m high, with a SW vergence within a volcanic region northwest of Pityusa Patera. Topographic profiles across the structure indicate that the northern part is higher and narrower in cross section than the southern part. Because the depth of faulting is deeper when the distance between the leading and the trailing syncline is longer (Grott et al., 2007), we have chosen a topographic profile in the southern edge of the structure in order to model the depth of faulting and obtain information about the BDT depth. There is an elongated depression just at the base of the scarp front (see Figs. 2 and 3); this depression is bounded by the own Pityusa Rupes front and by a lower scarp to the SW, which could be structurally controlled since it relatively linear. This depression would not modify the topography above Pityusa Rupes, but it is so close to the lobate scarp that the floor and the wall of the basin could be confused with the wall and the foot of the lobate scarp, and therefore we have included the basin in the profile in order to avoid this mistake.

Chalcoporos Rupes (numbered as 2 in Fig. 1 and Table 1) is located north of Pityusa Rupes. This scarp is about 260 km long, 700 m high and has a SW-NE trend (Fig. 2b). It is difficult to find topographic profiles across Chalcoporos Rupes suitable to use in the modeling process. The northern and the central areas of Chalcoporos Rupes are complex regions affected by impact craters and other structures, which prevent us from obtaining good models to

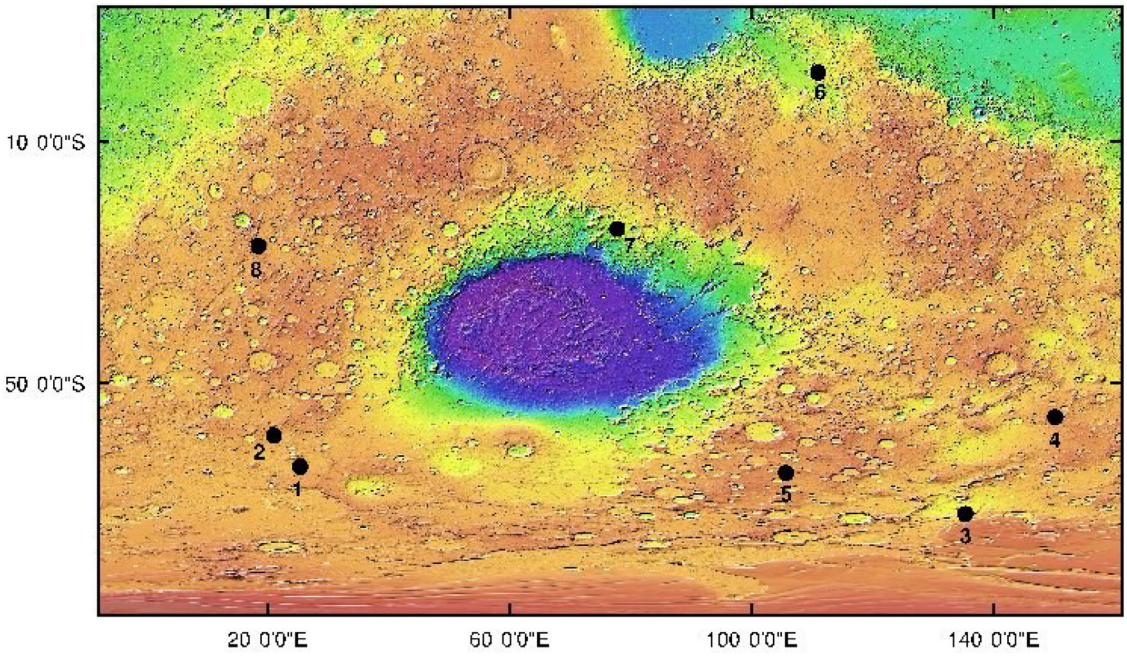

Fig. 1. Locations of lobate scarps studied in this work. The image is a MOLA Digital Elevation Model in Simple Cylindrical projection and 128 px/degree.

Table 1
Lobate scarp characteristics. Ages of each structure are calculated in Section 2.

	Lobate scarp	Location	Length (km)	Height (m)	Age (Ga)
1	Pityusa Rupes	25.4°E, 63.9°S	150	600	3.5–3.6
2	Chalcoporos Rupes	21.0°E, 58.7°S	250	700	3.9
3	Thyles Rupes	135.4°E, 71.7°S	263	1600	3.8
4	Lobate scarp 4	150.2°E, 55.7°S	170	900	3.7–3.9
5	Lobate scarp 5	105.8°E, 64.9°S	250	350	3.9
6	Amenthes Rupes	111.0°E, 1.4°N	420	1000	3.6–3.7
7	Lobate scarp 7	77.8°E, 24.5°S	210	300	3.4–3.5
8	Lobate scarp 8	18.6°E, 27.3°S	130	800	4.0

the topography. Therefore, we have placed the topographic profile in the southern extreme. This area is free of impact crater, but is affected by a regional slope that spreads beyond the scarp. In order to remove the slope from the topographic profile, we have assumed that a simple function of the type $y = a + bx + c/[(x-d)/f]^2$ would fit the topography reasonably well, $c/[(x-d)/f]^2$ is a good approximation for the topography of a fault, and bx takes into account the slope. The parameters a, b, c, d and f are calculated through a fit between our data and the function, and then we remove the slope from the profile. We obtained a slope of about 0.3% in this profile. Fig. 3 shows the already detrended topography. Images and analysis of topographic profiles across Chalcoporos Rupes placed in different regions along the structure show a variation in its dip after transecting an older impact crater, such that the northern region of the scarp shows a quite symmetric topographic profile with a slight SE vergence, while the southern part verges toward NW. This variation could indicate a transition to a high relief ridge-like structure, as has been seen on Mercury.

Thyles Rupes (numbered as 3 in Fig. 1 and Table 1) is about 160 km long and 1.6 km high. It has a SSW–NNE trend, and we distinguished a WNW vergence (Fig. 2c) after studying topographic profiles located at different regions of the structure. The area around Thyles Rupes shows a regional slope where a complicated set of scarps and wrinkles ridges are placed. Thyles Rupes transects an impact crater; the inclination of the crater's floor and crosscutting relationships suggest that this crater is younger that the regional slope, but older than the lobate scarp. Thus, the lobate scarp formation took place after the slope emplacement. This underlying crater alters the shape of the structure, so that the part of the lobate scarp that goes through the crater interior is lower and wider than the scarp exterior to the crater. The southern backslope of the lobate scarp is affected by a group of faults with different vergence directions, while the central and northern backslope are affected by a subcircular structure, which could be a degraded crater or terraced terrains, of about 150 km of diameter (see Fig. 2c). In order to model the depth of faulting, we have taken a topographic profile in the northern region. This profile avoids the structures in the back of Thyles Rupes and the deformation due to the crater, but runs across the terraced terrain, which could mask the trailing syncline position. We obtained a slope of 0.8% that was removed from the profile. Fig. 3 shows the topographic profile without the regional slope.

Lobate Scarp 4 is a SW-NE trending and a NW-vergin structure (Fig. 2d) located SE of Hellas rim. This lobate scarp is 170 km long and about 900 m of relief. The region where the structure is located shows a set of similar structures that runs parallel to the lobate scarp, such as Thyles and Ulyxis Rupes and Eridania Scopulus, together with multiple wrinkle-ridge rings, which are circular ridges that outline ghost craters. They are common structures in mare basalt units in the Moon and Mercury (e.g. Watters et al., 2009; Head et al., 2008; Klimczak et al., 2012).

Lobate Scarp 5 is an EW-trending structure that has a southward vergence (Fig. 2e), and is located in the main SE rim of Hellas. It is about 250 km long and 350 m high. Topographic pro-

files across the structure show the typical asymmetric morphology of lobate scarps. The topographic profile selected to model the depth of faulting is placed near two craters. However, the analysis of different topographic profiles across these craters ensures that the ejecta material does not significantly modify the shape of the structure; topographic profiles across the craters and perpendicular to the profile shown in Fig. 2e have a very flat topography until they reach the crater rims, where the crater basins start. So ejecta material does not seem to modify the topography significantly. Furthermore, the topographic profile used in the modeling process (Fig. 3) does not show evidence of deformation due to craters.

Amenthes Rupes (numbered as 6 in Fig. 1 and Table 1) is, as previously mentioned, the largest lobate scarp on Mars (Watters and Robinson, 1999). This structure is ~420 km long and ~1 km high, trends SE-NW and has a SW vergence (Fig. 2f). The region where the structure is located shows a regional SSW slope, but the selected MOLA profile has a very slight slope and a slope trend subtraction is therefore not necessary for the modeling process.

Lobate Scarp 7 is 250 km long and 300 m high. It has NS orientation and westward vergence (Fig. 2g). As mentioned above, this structure is the nearest to the internal scarp basin, and is the only one that is radial to the basin. The region around this fault is heavily cratered. Most topographic profiles are affected by other structures and tectonic features. Furthermore, there is a steep regional slope in the southern edge of the lobate scarp that is hard to remove due to the complexity of the area. Therefore the used MOLA profile has been taken in the northern side, where topography in the back of Lobate Scarp 7 is modified by several craters (Fig. 3). The trailing syncline of the lobate scarp is not useful to model the depth of faulting because it is masked by the ring of a bigger crater.

Lobate Scarp 8 is 130 km long, 800 m high, trends NS and has a westward vergence. The structure is within a complex area. It crosses a small crater; offsets in wall and floor materials in this crater indicate that Lobate Scarp 8 is a thrust fault (Fig. 2h). Also, MOLA topography across the structure shows the usual asymmetric profile that characterizes most lobate scarps.

Finally, we have obtained absolute model ages for the studied lobate scarps using the buffered crater counting technique and the database of martian craters ≥1 km of Robbins and Hynek (2012). The buffered crater counting technique, developed to determine the crater-based formation ages of linear or curvilinear features (e.g., Tanaka, 1982; Fassett and Head, 2008; Kneissl et al., 2015), was applied using the CraterTools software by Kneissl et al. (2011) using a buffer width of one crater radius around the

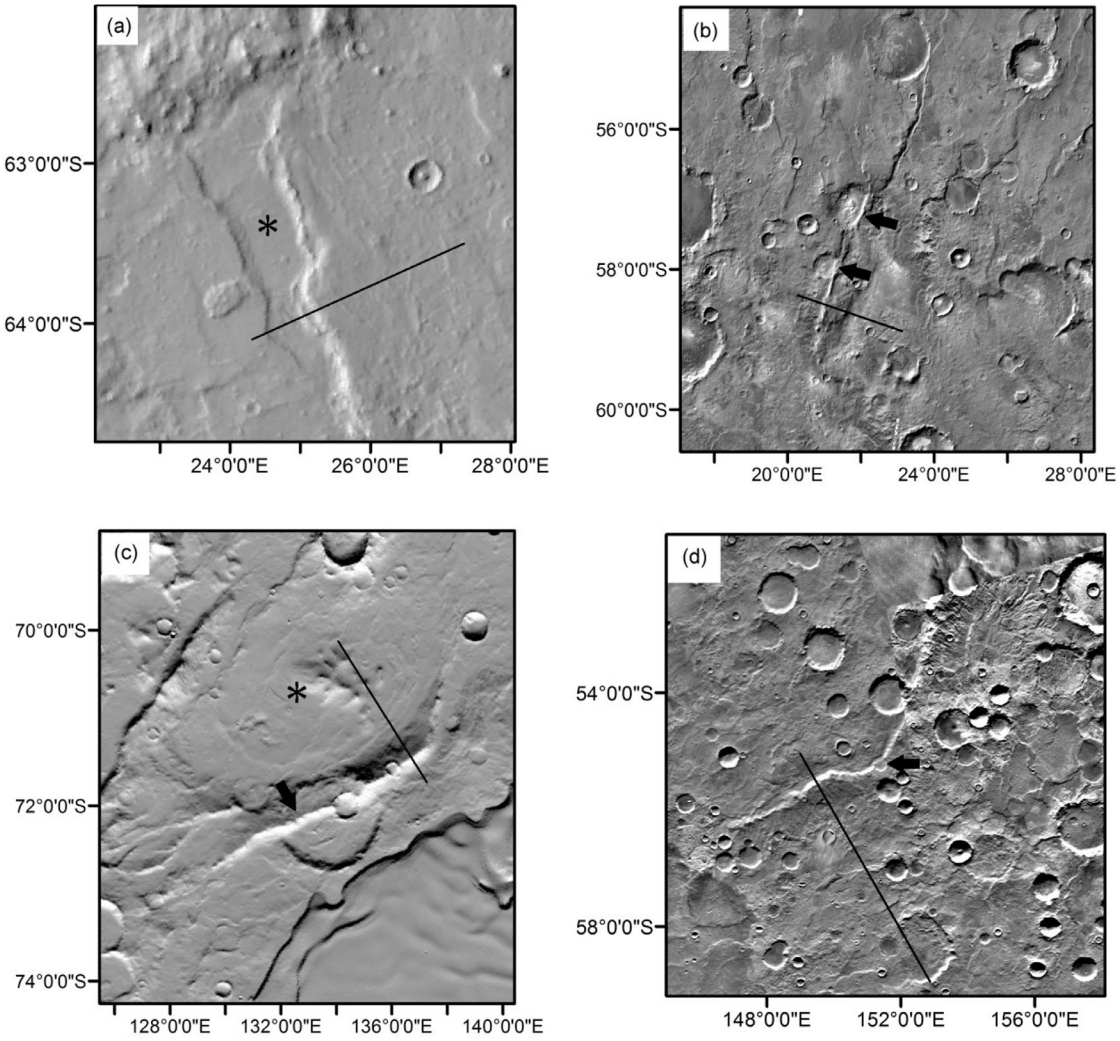

Fig. 2. (a) Pityusa Rupes, (b) Chalcoporos Rupes, (c) Thyles Rupes, (d) Lobate Scarp 4, (e) Lobate Scarp 5, (f) Amenthes Rupes, (g) Lobate Scarp 7 and (h) Lobate Scarp 8. Location of the topographic profile used in the modeling procedure is indicated with a black line. Arrows point out crosscut craters that have been shortened by lobate scarps. The asterisk shows the locations of the basin next to Pityusa Rupes (Fig. 2a) and the subcircular structure at the back of the Thyles Rupes (Fig. 2c). Figures (a), (c), (d) and (e) are obtained from a MOLA 1/128° digital elevation model. Figures (b), (f), (g) and (h) are a THEMIS (Thermal Emission Imaging System) 100 m/px mosaic.

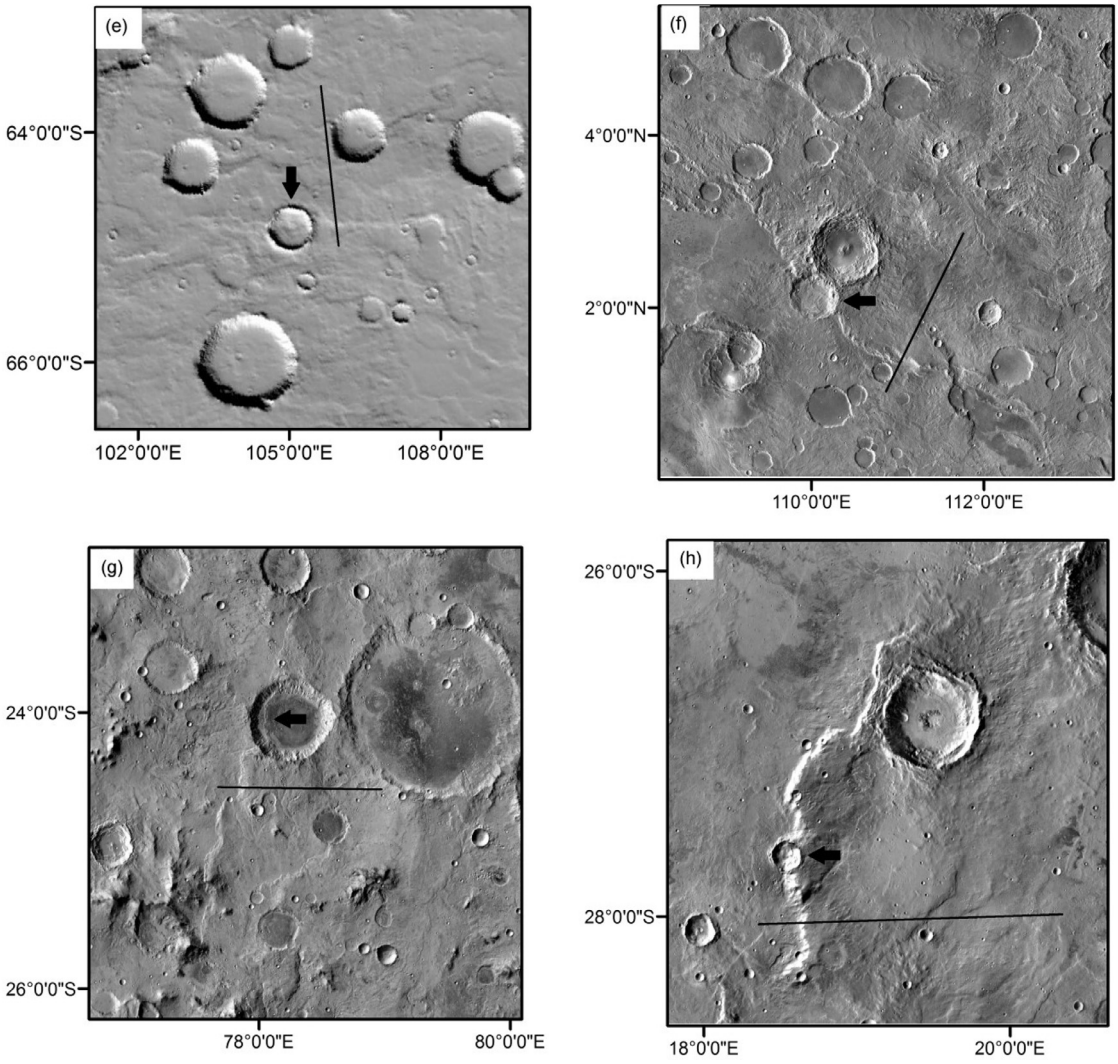

Fig. 2. Continued

scarps. The results were exported into the Craterstats software of Michael and Neukum (2010) and model ages of the lobate scarps were calculated from the crater size-frequency distributions using the production and chronology functions of Hartmann (2005) and Ivanov et al. (2001). Table 1 summarizes best-fit ages for each lobate scarp and isochrones are shown in Figs. 4 and 5; scarps with a range of ages listed in Table 1 reflect the difference in model ages derived from the two production and chronology functions.

3. Thrust fault modeling

In order to obtain the BDT depth beneath lobate scarps, we have used the mechanical dislocation program Coulomb (Toda et al., 2005). This program calculates surface deformation due to a fault by assuming that the lithosphere is an elastic, homogeneous and isotropic half-space. Faults are modeled through a rectangular geometry that is characterized by the sense and magnitude of slip, dip angle, fault depth and fault length. Surface deformation due to the fault is calculated by using the dislocation formalism of Okada (1992).

Coulomb allows us to know the fault slip, the dip angle and the depth of faulting by modeling the topography across a lobate scarp through a forward modeling procedure. Firstly, we specify in the model the set of parameters that characterize the fault and the medium: dip angle, vertical depth of faulting, fault slip and elastic constants. Then the material displacements are determined by following Okada (1992) equations. Finally, predicted topography provided by Coulomb is compared with observed topographic profiles across the lobate scarp. Best visual fits allows us to identify a narrow range of admissible fault dips, depths and displacements. This method has been used previously in other works to obtain the BDT depth beneath lobate scarps (e.g., Schultz and Watters, 2001; Watters et al., 2002; Ruiz et al., 2008; Egea-Gonzalez at al., 2012). Previous works evaluate the best fit models through standard deviation values (Egea-Gonzalez et al., 2012; Klimczac, 2014; Nahm and Peterson, 2016). This procedure gives good results when measured topographic profiles are relatively free of other structures and craters. However, if the topographic profile is affected by structures that are not related with the lobate scarp, then standard deviation values will provide as best modeled profiles those that also model the unrelated features (see Egea-Gonzalez et al., 2012 and Klimczac, 2014). Some of the topographic profiles used in this work are affected by structures that are not related to the fault, so we have ruled out the standard deviation method and have determined our results through good visual fits.

For the values of the elastic parameters, we assumed Young's modulus of 100 GPa and Poisson's ratio of 0.25 (Hauck et al., 2004). Reasonable variations in these parameters do not produce signifi-

cant variations in the results (see also Watters et al., 2002; Grott et al., 2007; Ritzer et al., 2010). Initial dip angle, displacement and depth of faulting are firstly estimated from, respectively, the slope of the backlimb, the maximum relief and the trailing syncline position. We have analyzed modeled topography produced by dip angles between18° and 48°, depth of faulting between 10 and 45 km, and displacements between 350 and 2100 m. Roughly, in the elastic model, higher dip angles give steeper topography, higher displacement values involve higher relief, and deeper structures increase the distance between the leading and the trailing syncline (see Schultz and Watters, 2001). Although the elastic modeling is an appropriate starting point to model the surface topography associated with long-term deformation that arises from cumulative fault offsets (e.g., King et al., 1988; Taboada et al., 1993; Cohen 1999), this method does not account for plastic deformation, therefore some discrepancies between modeled and measured topography are expected. Furthermore, the forward modeling method does not provide a unique solution, so we have chosen wide intervals of parameters that match topography reasonably well. The range in depth of faulting is used for surface heat flow calculations, so a range of surface heat flow is obtained that takes into account the uncertainty in the depth of faulting solution.

Topographic profiles across each lobate scarp have been derived from Mars Orbiter Laser Altimeter (MOLA) 1/128° digital elevation model (available at http://pds-geosciences.wustl.edu/missions/mgs/megdr.html). We have tried to choose MOLA profiles as representative of the structure as possible by avoiding impact craters, regional slopes and effects due to reasons that cannot be attributed to the fault. Topographic profiles are long enough to show the total extension of the fault and possible key structures that could affect our results.

The trailing syncline indicates the location of the lower fault tip, so the distance between the leading and the trailing syncline has a major influence on the derived depth of faulting; given a dip angle, longer distance provides deeper structures. For this reason, MOLA profiles are perpendicular to the structure and have been obtained from a two-point equidistant projection. However, this distance is not always useful to obtain the depth of faulting because modifications due to craters, other structures or younger material emplacements can mask the trailing syncline. Furthermore, in some

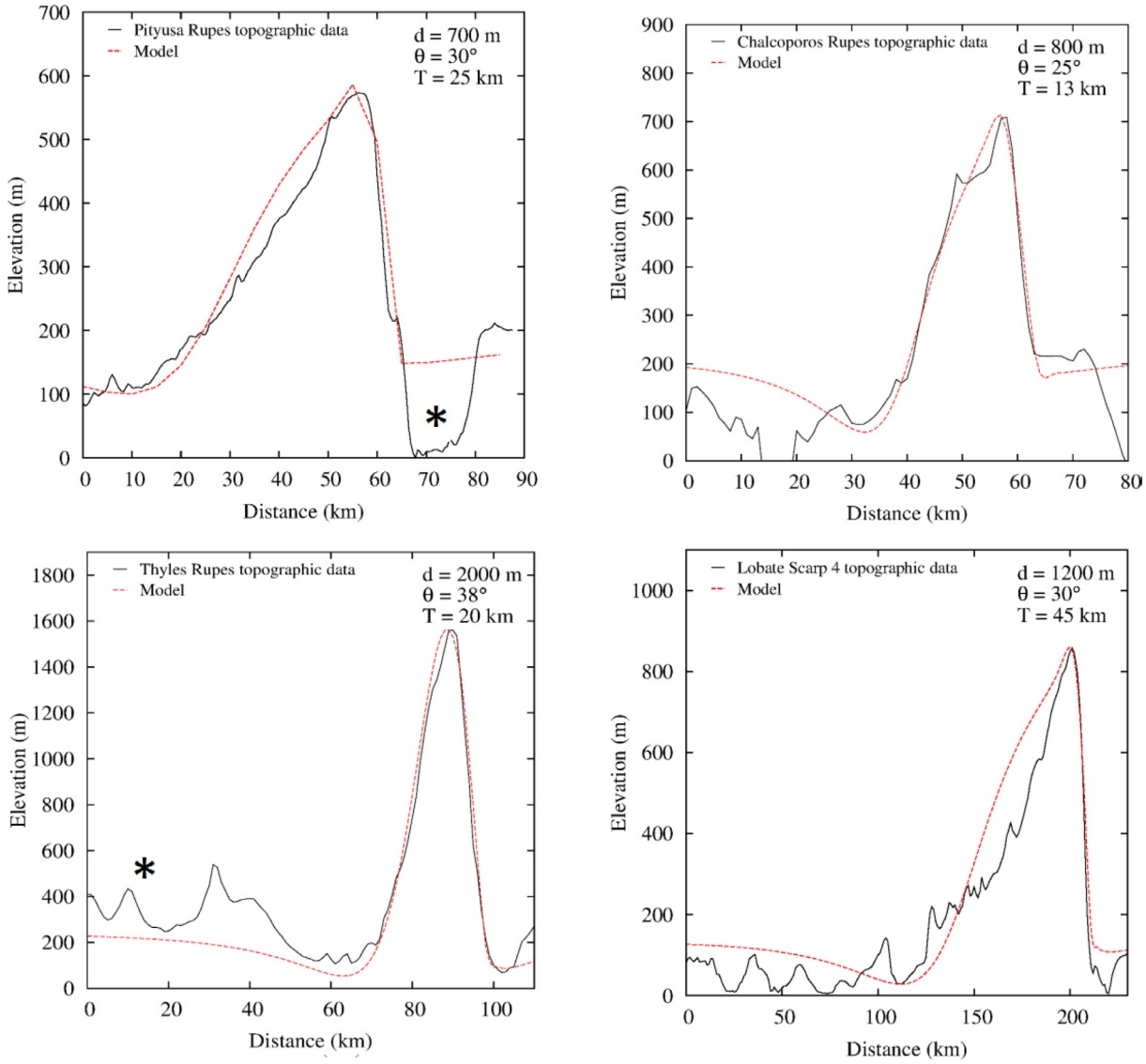

Fig. 3. Comparison between the MOLA topographic profiles (black) and modeled results (red). Model parameters are indicated in the upper right corner: d is displacement, θ is dip angle, and T is depth of faulting. The asterisk indicates the basin position in Pityusa Rupes and the subcircular structure in Thyles Rupes. (For interpretation of the references to colour in this figure legend, the reader is referred to the web version of this article.)

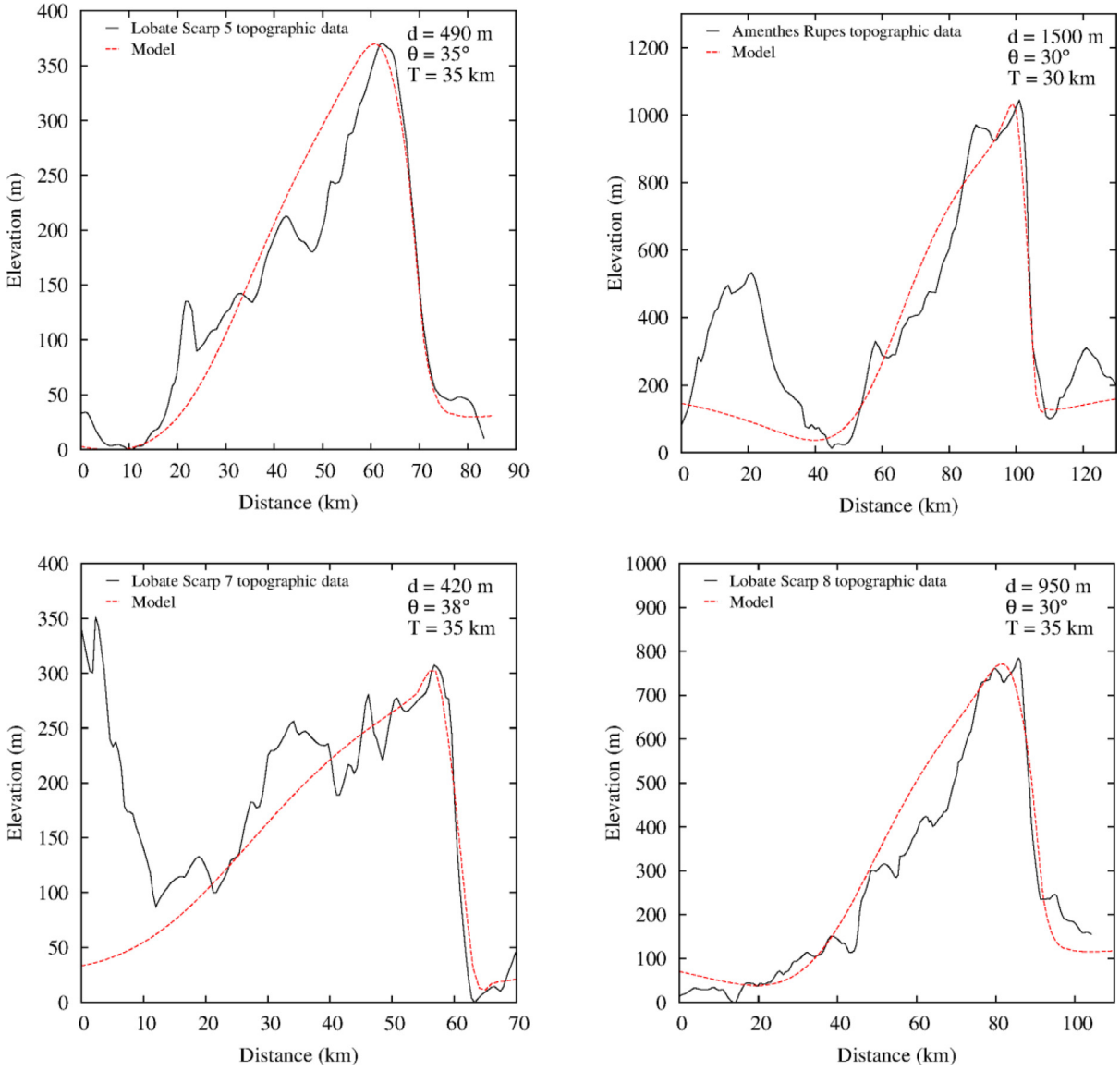

Fig. 3. Continued

structures, younger terrain seems to pool in the scarp face (Tanaka et al., 2014), so the vertical position of the foot wall is also distorted, affecting the displacement accommodated by the modeled fault. Nevertheless, good fits to the topography can be obtained in these cases by modeling the general shape across the lobate scarp. Keep in mind that our goal is not to model every single feature in the topographic profile, but those that are attributed to the fault and give information about the depth of faulting. Also, note that erosion rates are low in Mars (Golombek and Bridges, 2000), so we can assume that measured topographic profiles reproduce the topography across lobate scarps reasonably well at the formation time.

The distribution of displacement along the fault affects the shape of the modeled topography. Coulomb allows the specification of a tapered slip distribution in the strike and dip directions. We have found that best fits between measured and modeled topographic profiles are provided by elliptical slip distributions in any case. Best results are obtained with linear taper of 3 to 10 km on faults tips. Comparison between MOLA topography and best modeled topographic profiles is shown in Fig. 3. Table 2 summarizes the fault parameters obtained for each lobate scarp.

The MOLA profile used for Pityusa Rupes shows a basin next to the scarp front that has not been taken into account when seeking suitable modeled profiles. We have determined fault parameters that reproduce well the trailing syncline and the back of the scarp. Above the depression, we assume the same floor level that is found beyond the basin. Best modeled topographic profiles are obtained with fault slips between 680 and 700 m, dip angles that range between 30° and 40° and depth of faulting of 25–33 km.

After removing the regional slope from the topographic profile across Chalcoporos Rupes, we have obtained best fits through faults with slips of 700–900 m, dip angles of 25°–35° and depths of 13–17 km.

The Thyles Rupes area is heavily cratered. We have extracted the MOLA profile outside craters; however we could not avoid the terraced terrain at the back of the scarp, so the trailing syncline position is not useful to obtain the depth of faulting. As with Chalcoporos Rupes, topography shows a regional slope that has been eliminated. Good fits are obtained with a fault slip interval of 1900–2100 m, dip angles that range between 33° and 40° and depths of 15–20 km.

Table 2
Fault parameters obtained through Coulomb program and surface heat flow intervals. Calculations have been performed with pore pressure values between 0 and 0.35.

	Lobate scarp	Fault slip (m)	Dip angle (°)	Depth of faulting (km)	Surface heat flow (mW/m^2)
1	Pityusa Rupes	680–700	30–40	25–33	27–39
2	Chalcoporos Rupes	700–900	25–35	13–17	44–70
3	Thyles Rupes	1900–2000	33–40	15–20	38–61
4	Lobate Scarp 4	1100–1200	30	45	25–30
5	Lobate Scarp 5	470–500	32–38	33–38	27–33
6	Amenthes Rupes	1500–2000	20–35	27–33	27–37
7	Lobate Scarp 7	400–450	35–39	33–38	25–32
8	Lobate Scarp 8	950–1000	30–38	30–35	28–36

Results for the fault beneath Lobate Scarp 4 provide best fits between measured and modeled topography through a dip angle of 30°, a depth of faulting of 45 km and slips that range between 1100 and 1200 m. In the case of Lobate Scarp 5, MOLA topography matches to modeled profiles that are obtained from fault slips in the interval 470–500 m, dip angles that vary between 32° and 38° and depths of faulting of 33 and 38 km.

Amenthes Rupes topography is modeled with faults slips of 1500–2000 m, dip angles of 20°–35° and depths of faulting of 27–33 km. Although the area has a regional SSW slope, the selected MOLA profile shows a very slight slope and a subtraction is not necessary. As mentioned before, Amenthes Rupes has been studied previously by other authors. Location and orientation of topographic profiles differ in these studies; however differences in topography are minor, resulting in similar solutions when the elas-

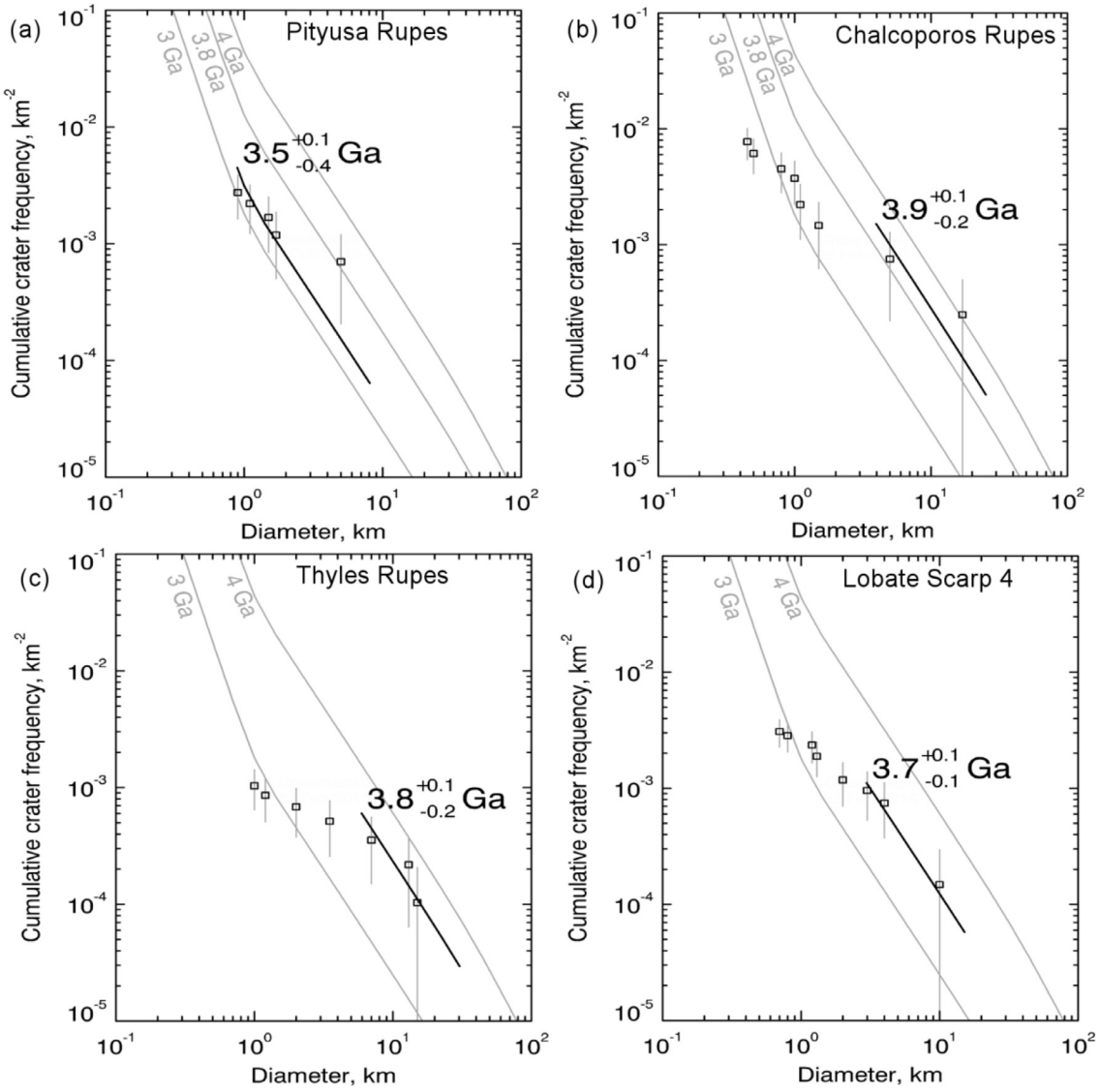

Fig. 4. Cumulative crater size–frequency distributions and derived absolute model ages for the eight studied lobate scarps. Model ages were derived using the production and chronology functions of Hartmann (2005).

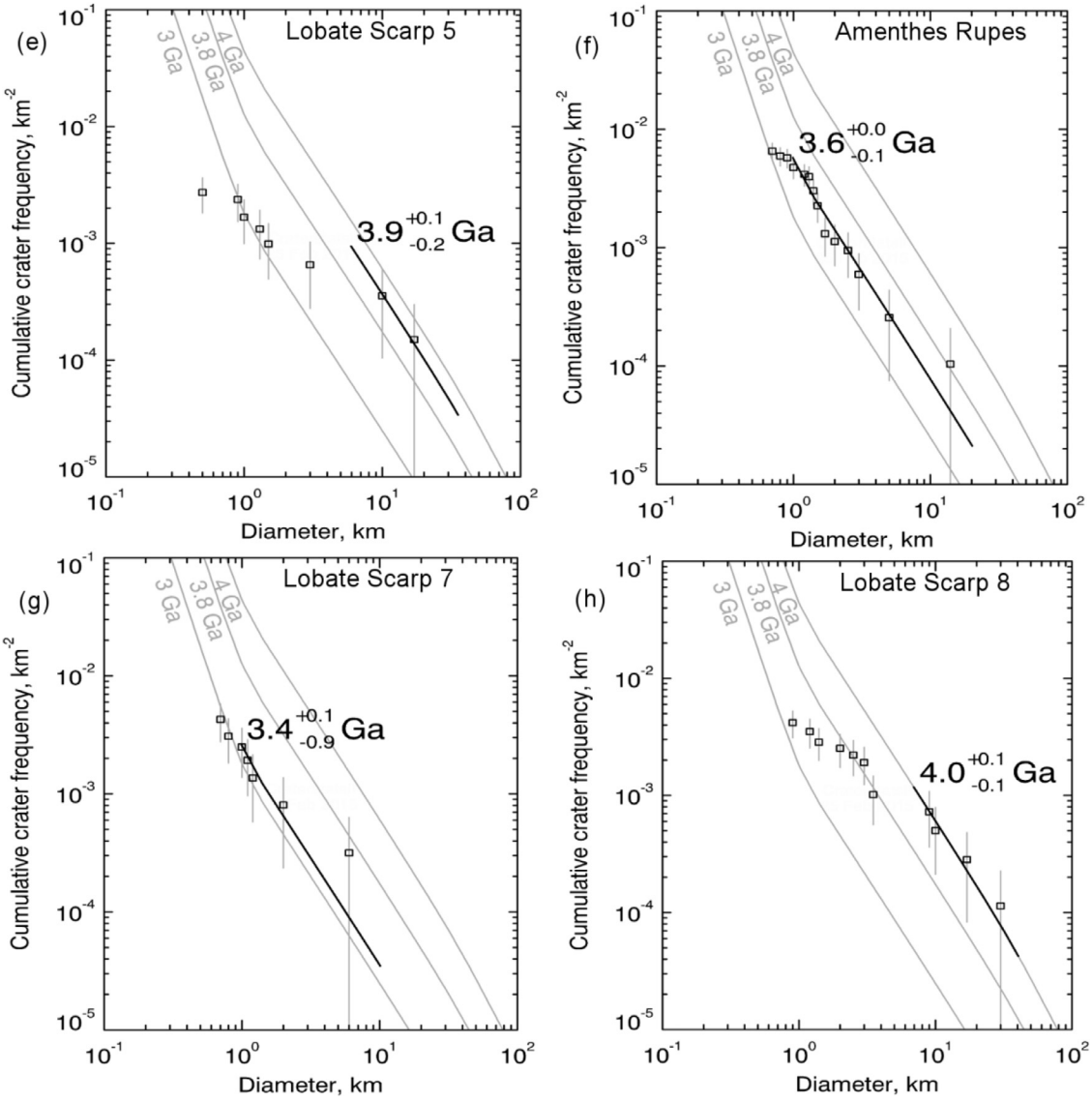

Fig. 4. Continued

tic model is applied. In this way, fault parameters obtained here are similar to those previously found through an elastic model by Schultz and Watters (2001) and Ruiz et al. (2008). However, comparison with results obtained by Mueller et al. (2014) shows more significant differences. These authors concluded that Amenthes Rupes is a listric fault with a depth of faulting of 33–48 km deep and a dip angle of 41.5°–56.1° by applying the fault-related fold theory, which takes into account plastic deformation. Although there are some differences in fault parameters due to the application of different methods, the depth of faulting provided by Mueller et al. point to a deep brittle-ductile transition, which is in line with our results.

Topography around Lobate Scarp 7 is complex. The back of the lobate scarp and the trailing syncline depression are modified by craters (see Fig. 2g and Fig. 3). The best fit for this topography has been obtained by ignoring these features and following the natural shape of the back. Best modeled profiles are provided by faults that are 33–38 km deep, slips of 400–450 m and dip angles of 35°–39°. However, notice that the topographic profile is so affected by other tectonic features that modeled parameters must be seen with caution. Modeled topography that fits MOLA data across Lobate Scarp 8 has displacements between 950 and 1000 m, dip angles that range between 30° and 38° and depth of faulting that varies between 30 and 35 km.

4. Heat flow calculations

Surface heat flows can be calculated from the depth of the faults associated with lobate scarp (e.g., Grott et al., 2007; Ruiz et al., 2008, 2009). The cold upper part of the lithosphere is a brittle layer where faulting is the prominent deformation mode, while at greater depth temperature increases and rocks have a ductile behavior under stress (e.g., Ranalli, 1997). Previous works assert that faults associated with lobate scarps develop in the brittle lithosphere until they reach the ductile region (e.g., Schultz and Watters, 2001; Watters et al., 2002). Therefore, depth of faulting indicates the brittle-ductile transition depth (Z_{BDT}). Because the ductile strength of the lithosphere depends on temperature, knowledge of Z_{BDT} allows heat flows to be calculated at the time of faulting.

The critical stress difference $(\sigma_1 - \sigma_3)$ that is necessary to cause faulting in the brittle lithosphere is given by (e.g., Ranalli, 1997)

$$(\sigma_1 - \sigma_3)_b = \alpha \rho g z (1 - \lambda); \quad (1)$$

where the subscript b indicates brittle regime, λ is the pore fluid pressure, ρ is the density, g is acceleration due to the gravity (3.72 m s^{-2}), and z is the depth. The coefficient α depends on the stress regime and takes a value of 3 in the case of thrust faulting (e.g., Ranalli, 1997). Previous works have reported the presence of water in the circum-Hellas region (Crown et al., 2005), so we have taken λ in the interval between 0 and 0.35, which is valid for dry (lower bound) and hydrostatic (upper bound) conditions. In the ductile regime, the stress differences needed to have a steady-state strain rate ε' is given by (e.g., Ranalli, 1997)

$$(\sigma_1 - \sigma_3)_d = \left(\frac{\varepsilon'}{A}\right)^{\frac{1}{n}} exp\left(\frac{Q}{nRT}\right). \quad (2)$$

where the subscript d indicates ductile regime, A and n are laboratory-determined constants, Q is the activation energy of creep, R is the gas constant (8.3145 J mol^{-1} K^{-1}), and T is the absolute temperature. Brittle and ductile strengths are equal at Z_{BDT}, thus we can obtain the temperature at this depth (T_{BDT}) from

$$T_{BDT} = \frac{Q}{nR}\left[ln\left(\frac{(1-\lambda)\alpha\rho g Z_{BDT}}{(\varepsilon'/A)^{1/2}}\right)\right]^{-1}. \quad (3)$$

In order to calculate T_{BDT}, we assume a crustal density of 2900 kg m^{-3}, which is suitable for a basaltic crust (e.g., Zuber et al., 2000; McGovern et al., 2002; Ruiz et al., 2008). Because there is much evidence of geological activity related to water, we have taken into account creep parameters appropriate for wet diabase: A = 0.0612 MPa^{-n} s^{-1}, n = 3.05 and Q = 276 kJ mol^{-1}

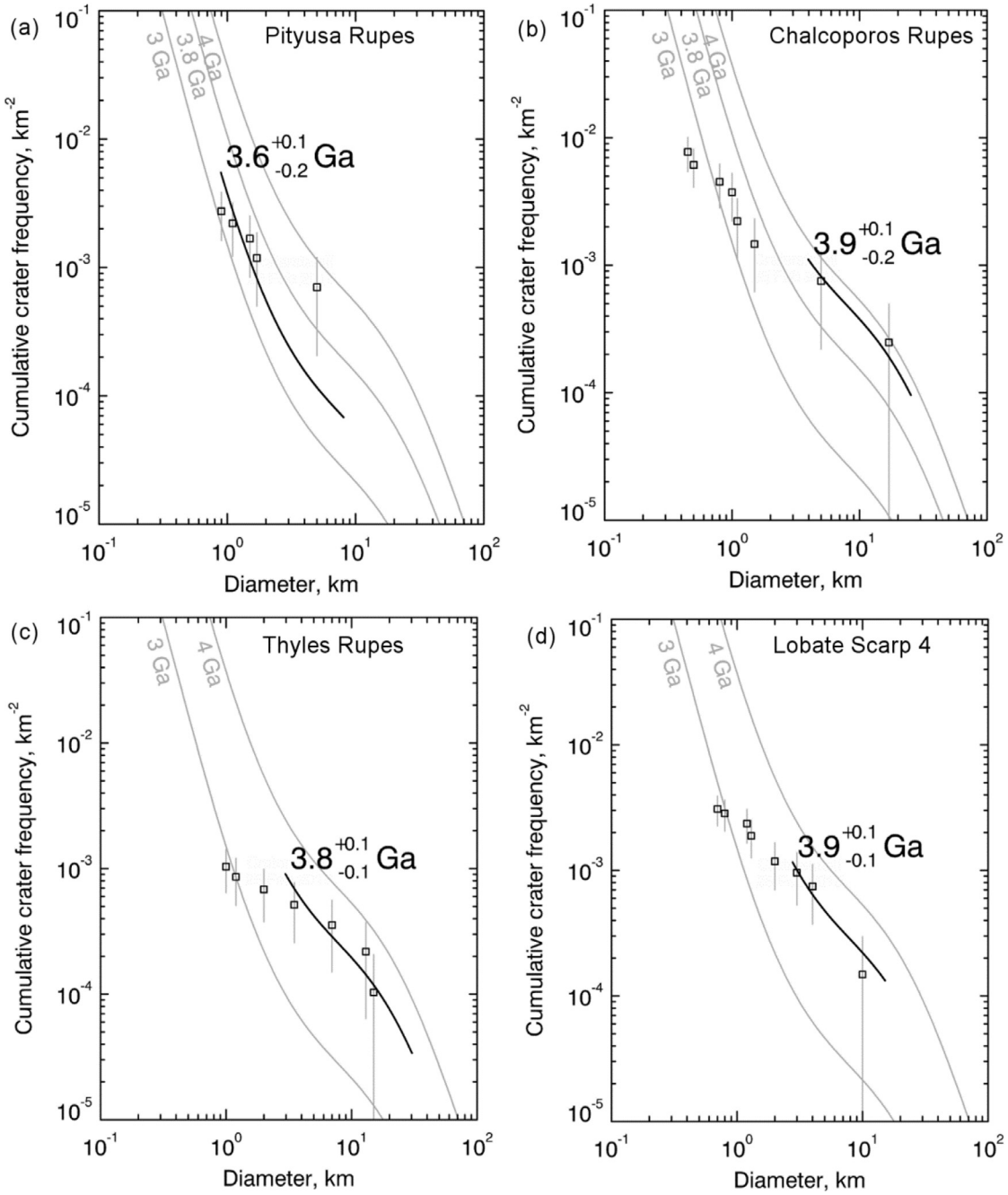

Fig. 5. Cumulative crater size–frequency distributions and derived absolute model ages for the eight studied lobate scarps. Model ages were derived using the production and chronology function of Ivanov et al. (2001).

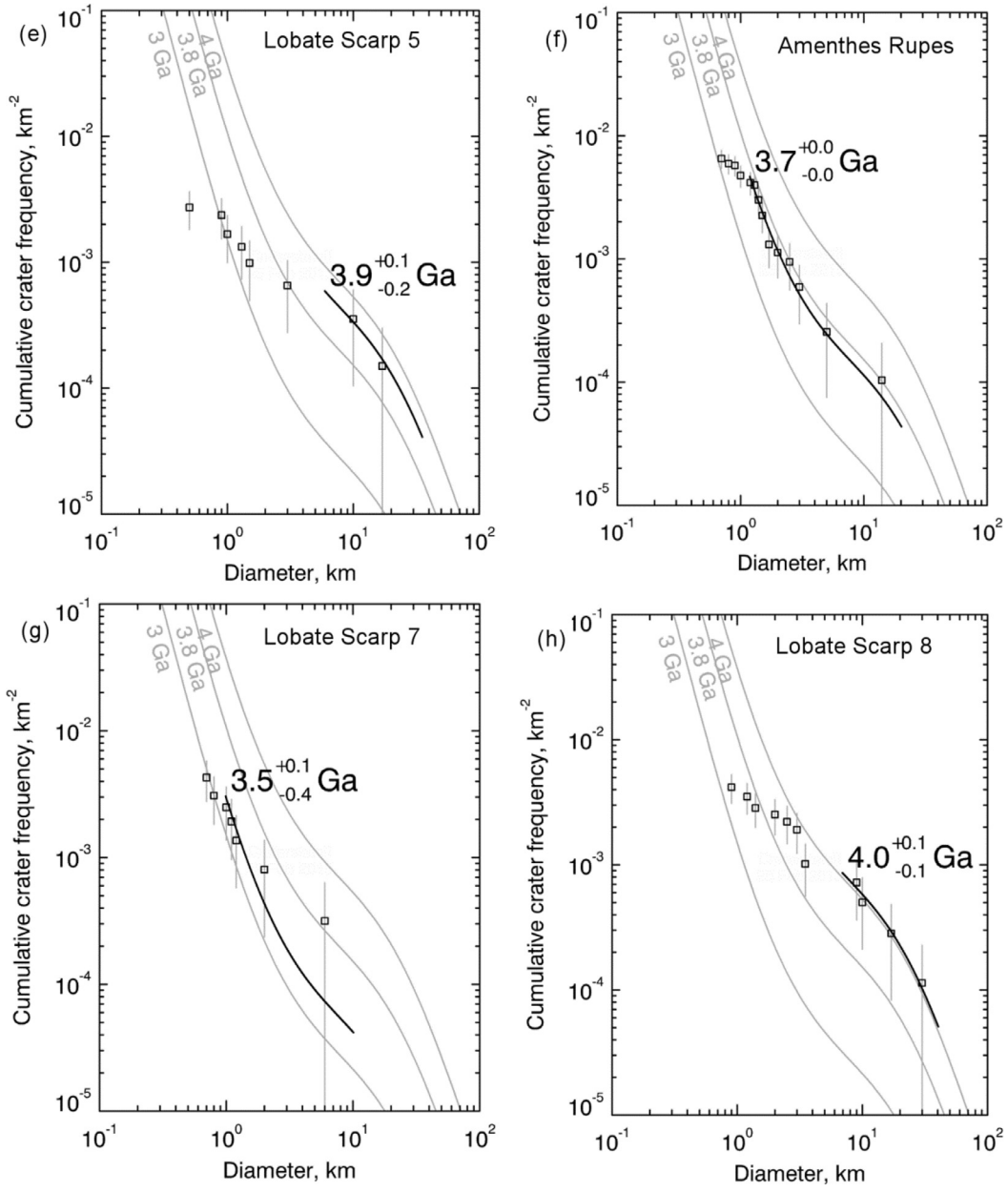

Fig. 5. Continued

(Caristan, 1982). Regarding strain rates, we have assumed the interval of 10^{-16} s^{-1} to 10^{-19} s^{-1} (see McGovern et al., 2002; 2004; Ruiz et al., 2011). The higher value is the typical strain rate of active terrestrial plate interiors, and the lower one is obtained by Schultz (2003) for the Amenthes fault population.

Surface heat flows (F_S) can be calculated from T_{BDT} through

$$F_S = \frac{k(T_{BDT} - T_S)}{Z_{BDT}} + \frac{Z_{BDT}H}{2} \quad (4)$$

this expression supposes steady state vertical heat conduction inside a layer with homogeneously distributed crustal heat sources (e.g., Carslaw and Jaeger, 1959; Ruiz et al., 2009), where k is the thermal conductivity of the layer, T_S is the temperature at the surface, and H is the volumetric heat production rate. We have performed calculations with constant thermal conductivity of 2 W m^{-1} K^{-1}, which is appropriated for intact, non-porous basaltic rocks (Beardsmore and Cull, 2001). Finally, we assume as T_S the present mean surface temperature on Mars, 220 K (e.g., Kieffer et al., 1977).

The radioactive heat production rate depends of the abundance of the heat-producing elements (HPEs) in the crust. HPEs are incompatible elements with tendency to accumulate on the magmas and to be more abundant in the uppermost part of the crust. Near surface K and Th abundances were measured by Mars Odyssey GRS (Boynton et al., 2007; Hahn et al., 2011), although good data south of Hellas basin is lacking, at latitudes southward 60° S, so there are no precise GRS estimates on heat production for some of the selected lobate scarps. Moreover, while it is true that on Mars HPEs abundance, and hence the radioactive heat production, varies from one area to another on the planet, in the southern highlands HPEs distribution is comparatively homogeneous and similar to global average values; this is also the case of the terrains surrounding Hellas where the lobate scarps studied here are located. Thus, we have opted to take as representative the average K and Th crustal abundances of, respectively, 3652 and 0.69 ppm (Hahn et al., 2011),

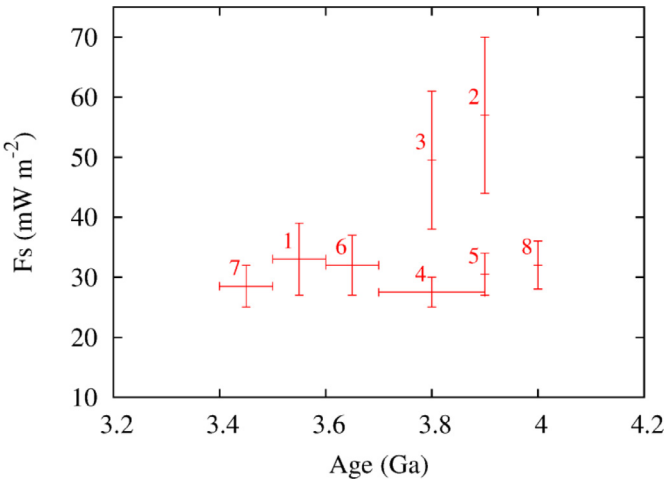

Fig. 6. Surface heat flows shown as a function of age.

whereas for estimating U abundance a Th/U ratio of 3.8 was assumed (e.g., Meyer et al., 2003). We also assume homogeneously distributed crustal heat sources in depth because ejected material from the Hellas basin and subsequent heavy cratering should have contributed to mixing of the uppermost crust (Taylor et al., 2006).

Surface heat flows are summarized in Table 2. Fig. 6 shows F_S as a function of the age for the analyzed lobate scaps for the wet diabase case. The obtained heat flows are quite uniform over the studied period. However, Chalcoporos and Thyles Rupis results are exceptions that give very high values (ranging from ~40 to ~60–70 mW m^{-2}). A large surface heat flow for Chalcoporos Rupes could be related to the volcanic activity located in Pityusa Patera around 3.8 Ga. However, the wide interval for possible values of F_S obtained in Chalcoporos Rupes and Thyles Rupes suggests uncertainty in fault modeling; in fact, the topography near both structures is affected by other structures (see Section 2), making modeled depths of faulting less reliable for both lobate scarps, which in turn could lead us to anomalously high surface heat flows. If we eliminate the results for Chalcoporos and Thyles Rupis, all the obtained surface heat flows are between 25 and 39 mW m^{-2}. These values agree with results obtained by Ruiz et al. (2011) for different regions on Mars, and indicate low surface heat flows in the circum-Hellas region for the studied period.

Recent work points to an ancient martian crust that could contain a substantial amount of felsic rocks (Carter and Poulet, 2013; Wray et al., 2013; Baratoux et al., 2014; Sautter et al., 2015). Thus, we also calculate heat flows by using a wet quartzite flow law (Koch et al., 1989), a thermal conductivity of 2.5 W m^{-1} K^{-1} (Beardsmore and Cull, 2001), and a density of 2750 kg m^{-3}, which are more appropriated for felsic material (Fountain et al., 1990), in order to show the case of an end-member felsic crust. In this case, we have obtained surface heat flows that range between 15 and 38 mW m^{-2} (but 15–23 mW m^{-2} if we ignore Chalcoporos and Thyles rupes; see above). These results are lower than those provided by wet diabase, but they are compatible with the lower bound results obtained by Ruiz et al. (2011). Previous comments about wet diabase results also apply to quartzite results: F_S values are low and uniform with the exceptions of Chalcoporos and Thyles Rupis. We notice that variations in density involve minor variations in surface heat flows (less than 3%), so we will keep 2900 kg m^{-3} as our nominal density.

5. Crustal thickness and heat flow in the circum-Hellas region

The Hellas impact basin, and associated rim, represents a major topographic excursion that dominates much of Mars' southern hemisphere topography (Smith et al., 1999). The material removed from Hellas also represents a major redistribution of Mars' early crust (Zuber et al., 2000; Neumann et al., 2004).

Crustal thickness models of Zuber et al. (2000) and Neumann et al. (2004, 2008) were constructed for a mean crustal thickness of ~45 km, which is a reasonable lower limit for a crustal nominal density of 2900 kg m^{-3}. However, previous estimations of effective elastic thickness and heat flow were performed for a mean crustal thickness of 50 km (McGovern et al., 2004; Ruiz et al., 2011), a value more consistent with geophysical evidence for the nominal density (Wieczorek and Zuber, 2004; McGovern et al., 2004; Ruiz et al., 2008; Ruiz et al., 2009). Thus, we have performed an independent calculation of the crustal thickness in this area assuming a mean crustal thickness of 50 km and a crustal nominal density of 2900 kg m^{-3}, in order to investigate the relation between faulting depth, heat flow and crustal thickness at the Hellas region.

We use the relationship between global topography and gravity data to model the crustal thickness (T_c) of Mars following the potential theory procedure of Wieczorek and Phillips (1998), which has also been used for previous crustal thickness modeling of Mars (e.g., Zuber et al., 2000; Neumann et al., 2004, 2008). To constrain the thickness of the martian crust, we assume (1) that the observed gravitational anomalies arise only from a combination of surface topography and variations at the crust-mantle interface (i.e., the "Moho"), and (2) constant crustal and mantle densities to overcome the non-uniqueness associated with potential modeling. We use the spherical harmonic model MarsTopo2600 of the shape of Mars from Wieczorek (2015), and the gravitational potential model JGMRO_110C from Konopliv et al. (2011). Topography data are useful only up to the resolution of gravity data, so both gravity and topography coefficients are truncated beyond degree and order 90 in our analysis given the dramatic decrease in spectral correlation that is observed between the observed gravity and topography beyond this degree (e.g., Baratoux et al., 2014). It is further required either to assume a mean crustal thickness or to anchor the inverted crustal thickness to a given value at a specific location (e.g., Wieczorek, 2015). As mentioned previously, our model assumes a mean crustal thickness of 50 km (that satisfy the condition that the inverted crustal thickness is not negative anywhere on the planet), and crustal and mantle lithosphere densities of, respectively, 2900 and 3500 kg m^{-3}, values widely used for Mars (e.g., Zuber et al., 2000; McGovern et al., 2004; Neumann et al., 2004; Ruiz et al., 2011). Under these assumptions, we first calculate the Bouguer gravity anomaly from surface topography and free air anomaly, and then calculate by downward continuation the shape of the crust–mantle interface necessary to minimize the difference between the observed and predicted Bouguer anomalies (for reviews see Wieczorek and Phillips, 1998; Wieczorek, 2015). In order to mitigate errors in downward continuing the Bouguer anomaly, we applied a minimum amplitude filter (see Wieczorek and Phillips, 1998) for the Moho relief at degree $l = 50$. Finally, we obtain the crustal thickness by subtracting the relief on the Moho from surface topography. The obtained crustal thickness model for the circum-Hellas region is shown in Fig. 7.

As seen in other major impact basins on Mars or the Moon, the crust is thinned beneath Hellas (thinner than 30 km), owing to a combination of excavation and mantle rebound during the impact process (Bratt et al., 1985; Zuber et al., 2000), and is surrounded by an annulus of thickened crust (thicker than 50 km), which constitutes the circum-Hellas region (see Fig. 7). As expected, our mean thickness of 50 km leads to slightly higher crustal thickness values than previous models constructed for a mean thickness of ~45 km

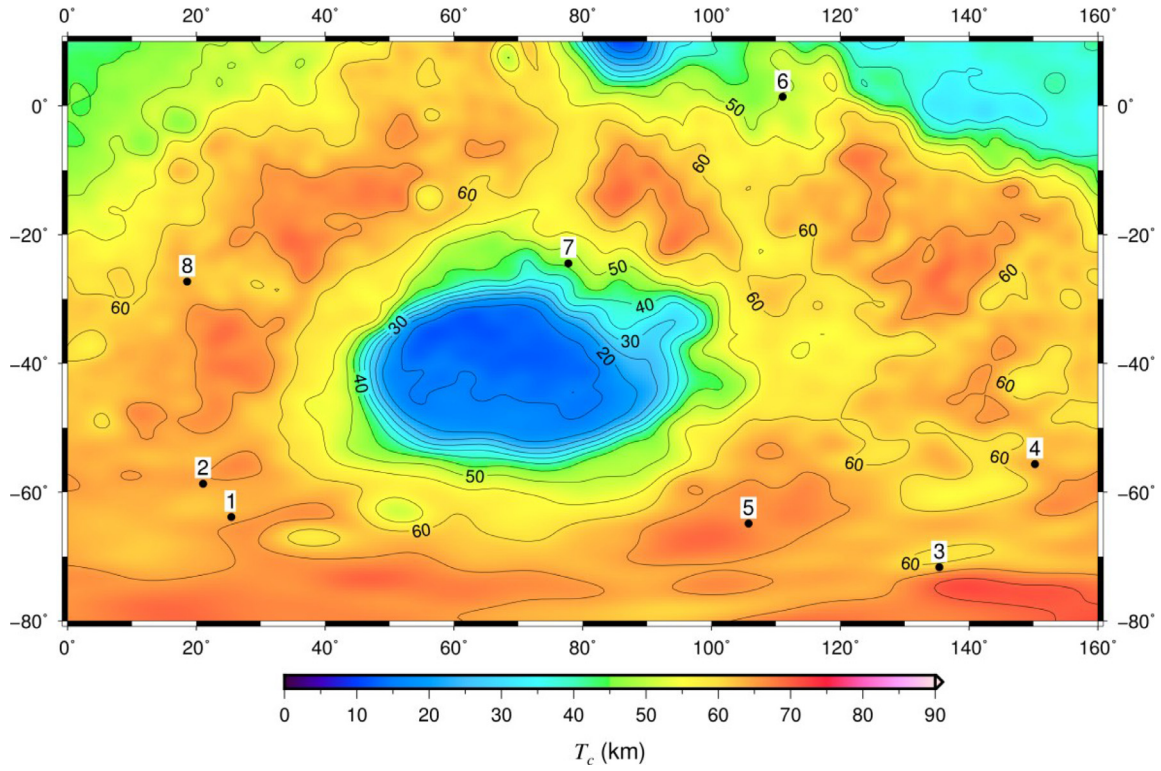

Fig. 7. Crustal thickness map for the circum-Hellas region, showing the locations of lobate scarps studied in this work. The model assumes a mean crustal thickness of 50 km, and crustal and mantle lithosphere densities of, respectively, 2900 and 3500 kg m^{-3}. The crustal thickness contour interval is 5 km.

(e.g., Zuber et al., 2000; Neumann et al., 2004, 2008). Note, however, that this difference is not homogeneous: the largest crustal thickness differences (>5 km) occur in the circum-Hellas region, whereas this difference decreases to <5 km in the Hellas basin.

6. Discussion: surface and mantle heat flows

Surface heat flows obtained in this work are similar to those obtained by Ruiz et al. (2011) from the effective elastic thickness and the brittle-ductile transition for several regions on Mars of similar age, including Amenthes Rupes and Hellas rim.

The F_S values obtained from strength estimation procedures are lower than those derived by most thermal history models, which, in general, obtain surface heat flows above 50 mW m^{-2} in the studied period (Hauck and Phillips, 2002; Williams and Nimmo, 2004; Grott and Breuer, 2010; Fraeman and Korenaga, 2010), but similar to the values obtained by the evolution model of Ruedas et al., (2013). This discrepancy between heat flow estimates based on lithospheric strength and thermal models has been previously noted (see Ruiz et al., 2011; Mueller et al., 2014), and could indicate inefficient mantle cooling, at least during some stages of martian evolution (Ruiz, 2014), which is consistent with several geological and geophysical studies (e.g., Yoder et al., 2003; Nahm and Schultz, 2011). Alternatively, low heat flows could be due to subchondritic HPEs abundances. In this sense, Phillips et al. (2008) suggest that the large effective elastic thickness found under north polar region could be compatible with sub-chondritic abundances of HPEs. Furthermore, Grott and Breuer (2009) studied different thermal evolution models compatible with large elastic thickness and concluded that a subchondritic heat production rate is necessary if the elastic thickness in the polar cap is representative for the bulk of the planet.

Previous work does not constrain heat flows in the Noachian-Early Hesperian period because most available effective elastic thicknesses are upper limits in this period (McGovern et al., 2004; Ruiz et al., 2011), and therefore lower limits for the heat flow were mostly calculated; the only upper heat flow limits calculated for this period were derived from the depth of faulting beneath Amenthes Rupes and two large lobate scarps in Thaumasia, and from the effective elastic thickness in Hellas South rim (e.g., Ruiz et al., 2011). Results presented in this work match with those previously obtained, and suggest that low heat flows could also extend into the Noachian period.

On the other hand, the surface heat flows obtained in this work for the circum-Hellas region are very similar for the majority of studied lobate scarps (with the exception of Chalcoporos and Thyles rupis), independently of time of feature formation and of local crustal thickness, which therefore implies that F_S and T_c are unrelated (Fig. 8). We can calculate mantle heat flows for each lobate scarp by means of the expression $F_m = F_s - T_c H$, where F_m is the total heat flow that comes from the mantle, which includes convective heat flow and radiogenic heat production in the lithospheric mantle. Excepting again Chalcoporos Rupes and Thyles Rupes, we have found very low mantle heat flows, reinforcing the evidence favoring limited mantle cooling, at least during some periods of the history of Mars (Ruiz et al., 2011; Ruiz, 2014). In some cases the so obtained mantle heat flows are even negative, which does not seem realistic. Thus, the total crustal production cannot be homogeneous in the whole crust, because it would imply a crustal, radioactively generated, heat flow component higher than the derived surface heat flow. Both the independence of the surface heat flow with crustal thickness and low mantle heat flows suggest therefore a stratified crust in the circum-Hellas area, with heat-producing elements concentrated in a layer thinner than the whole crust, which would be nearly homogeneous in thickness across the circum-Hellas region. Similar evidence has been found in previous works for Solis Planum and Thaumasia highlands regions (Ruiz et al., 2009).

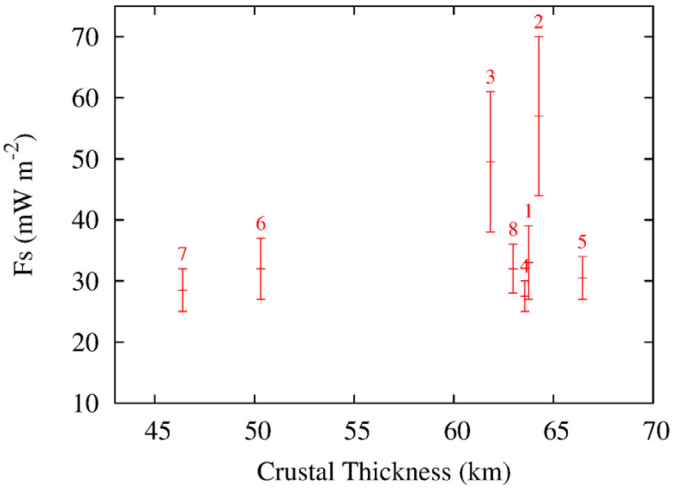

Fig. 8. Comparison of surface heat flows with crustal thickness.

Uniformity in results obtained in this work and the similarity with those provided by other authors in different regions for the same period suggests that formation and development of Hellas basin had minor influence on surface heat flows at the lobate scarp formation time and locations. Although thermal perturbation produced by a giant impact basin is highly unconstrained, our results agree with thermal perturbation models that suggest a probable cessation of thermal perturbation at the scarps location before their formation (Watters et al., 2009; Roberts et al., 2009).

The crust around Hellas basin is thickened by the emplacement of ejecta deposits with the result that studied lobate scarps are located in one of the areas of thick crust of Mars. As a consequence we would expect lower surface heat flows than in other regions, however, as has been mentioned before, uniformity in results points to no dependence with crustal thickness. Ejecta material at lobate scarp locations could form a fractured layer in the uppercrust. Fractured rocks have lower thermal conductivity, which involves higher temperatures and lower surface heat flows (Egea-González et al., 2014) than those calculated here, so our results are upper limits.

Some discussion about the martian crust composition and the implications that this entails for thermal mantle evolution is ongoing. Felsic rocks has been proposed as a major constituent in the martian crust (e.g., Baratoux, et al., 2014; Sautter et al., 2015) and new models of basalt formation have been implemented in order to determine conditions for magma formation and thermal evolution. Although detailed conclusions depend on constraints used in each study, in general simple convective cooling seems enough to explain crust composition (see Baratoux et al., 2011, 2013; Filiberto and Dasgupta, 2015). However crust composition is still under debate; Gazel et al. (2016) conclude that martian crust is mainly basaltic based on geochemical evidence. Furthermore, Rogers and Nekvasil (2015) indicate that thermal infrared (TIR) data do not support a felsic interpretation of near-infrared (NIR) spectral data and suggest a basaltic crust to explain results from TIR and NIR measurements. Besides, simple convection cooling does not provide an appropriate explanation for young shergottites, which have been dated from late-Amazonian (e.g., Nyquist et al., 1998, 2001; Moser et al., 2013; Bellucci et al., 2016). More recently, Sautter et al. (2016) studied the Noachian crust composition from orbital, in-situ and meteorite data, and concluded that mantle temperature increased from Noachian to Hesperian, which is in line with results obtained in this article.

Finally, although we would expect higher heat flows in volcanic regions around Hellas, we have obtained similar values of F_S in non-volcanic areas for a wide region. Such a uniform and low surface heat flow could fit with a one-plate planet and the existence of a poor heat conducting stagnant lid. Efficiency of heat transfer in the stagnant lid regime is much lower than in plate tectonics, which could explain low surface heat flows. Moreover, heat diffusion in the stagnant lid would attenuate heterogeneities coming from the mantle and may account for uniformity in our results (Grott and Breuer, 2010).

7. Conclusions

The depth of faulting beneath lobate scarps in the circum-Hellas region provides evidence for low surface and mantle heat flow in Noachian to Early Hesperian times, additionally supporting limited cooling of the martian interior. In addition to the implied low surface heat flows, the homogeneous pattern of surface heat flow is consistent with a one-plate planet experiencing stagnant lid convection. Moreover, obtaining greatly homogeneous surface heat flow independently of crustal thickness variations suggests crustal stratification including an upper layer enriched in HPEs. Therefore, our results for the circum-Hellas region solve key points on the structure of the martian crust, and help improve our understanding of the thermal state and internal evolution of the red planet in Noachian to Early Hesperian times.

Acknowledgements

Our crustal thickness model was obtained using the freely available software SHTOOLS (Wieczorek et al., 2016; available at https://github.com/SHTOOLS). Several figures were generated using the Generic Mapping Tools (Wessel et al., 2013). The work by J.R. was supported by a contract Ramón y Cajal at the Universidad Complutense de Madrid (UCM). The work by L.M.P. was supported by a FPU2014 grant from the Ministerio de Educación, Cultura y Deporte of Spain. The work by J.-P.W. was supported by a NASA Mars Data Analysis Program Grant No. NNX14AM12G. This work has received funding from the European Union's Horizon 2020 Programme (H2020-Compet-08-2014) under grant agreement UPWARDS-633127, and from the Spanish Ministry of Economy and Competitiveness Project CGL2014-59363-P (AMARTE). We are grateful to Amanda Nahm, and to an anonymous reviewer for their useful comments that helped in improving the manuscript.

References

Baratoux, D., et al., 2014. Petrological constraints on the density of the Martian crust.. J. Geophys. Res. 119, 1707–1727.
Baratoux, D., Toplis, M.J., Monnereau, M., et al., 2011. Thermal history of Mars inferred from orbital geochemistry of volcanic provinces. Nature 472, 338–341. doi:10.1038/nature09903.
Baratoux, D., Toplis, M.J., Monnereau, M., Sautter, V., 2013. The petrological expression of early Mars volcanism. J. Geophys. Res. 118. doi:10.1029/2012JE004234.
Beardsmore, G.R., Cull, J.P., 2001. Crustal Heat Flow: A Guide to Measurement and Modelling. Cambridge University Press, Cambridge, p. 324.
Bellucci, J.J., Nemchin, A.A., Whitehouse, M.J., et al., 2016. A Pb isotopic resolution to the Martian meteorite age paradox. Earth Planet. Sci. Lett. 433, 241–248.
Boynton, W.V., et al., 2007. Concentration of H, Si, Cl, K, Fe, and Th in the low and mid latitude regions of Mars. J. Geophys. Res. 112, E12S99. doi:10.1029/2007JE002887.
Bratt, S.R., Solomon, S.C., Head, J.W., 1985. The evolution of impact basins: cooling, subsidence, and thermal stress. J. Geophys. Res. 90 (B14), 12415–12433.
Caristan, Y., 1982. The transition from high temperature creep to fracture in Maryland diabase. J. Geophys. Res. 87, 6781–6790.
Carslaw, H.S., Jaeger, J.C., 1959. Conduction of Heat in Solids. Oxford University Press, London.
Carter, J., Poulet, F., 2013. Ancient plutonic processes on Mars inferred from the detection of possible anorthositic terrains. Nat. Geosci. 6, 1008–1012.
Chicarro, A.F., Schultz, P.H., Masson, P., 1985. Global and regional ridge patterns on Mars. Icarus 63 (1), 153–174.
Cohen, S.C., 1999. Numerical models of crustal deformation in seismic zones. Adv. Geophys. 41, 133–231.

Crown, D.A., Bleamaster III, L.F., Mest, S.C., 2005. Styles and timing of volatile-driven activity in the eastern Hellas region of Mars. J. Geophys. Res. 110, E12S22. doi:10.1029/2005JE002496.
Egea-González, I., Ruiz, J., Fernández, C., et al., 2012. Depth of faulting and ancient heat flows in the Kuiper region of Mercury from lobate scarp topography. Planet. Space Sci. 60, 193–198.
Egea-González, I., Ruiz, J., 2014. Influence of an insulating megaregolith on heat flow and crustal temperature structure of Mercury. Icarus 232, 220–225.
Fassett, C.I., Head, J.W., 2008. The timing of Martian valley network activity: constraints from buffered crater counting. Icarus 195, 61–89.
Fassett, C.I., Head, J.W., 2011. Sequence and timing of conditions on early Mars. Icarus 211, 1204–1214.
Filiberto, J., Dasgupta, R., 2015. Constraints on the depth and thermal vigor of melting in the Martian mantle. J. Geophys. Res. 120, 109–122. doi:10.1002/2014JE004745.
Fountain, D.M., Salisbury, M.H., Percival, J., 1990. Seismic structure of the continental crust based on rock velocity measurements from the Kapuskasing Uplift. J. Geophys. Res. 95 (B2), 1167–1186. doi:10.1029/JB095iB02p01167.
Freed, A.M., Melosh, H.J., Solomon, S.C., 2001. Tectonics of mascon loading: resolution of the strike-slip faulting paradox. J. Geophys. Res. 106 (E9), 20603–20620. doi:10.1029/2000JE001347.
Fraeman, A.A., Korenaga, J., 2010. The influence of mantle melting on the evolution of Mars. Icarus 210, 43–57.
Frey, H.V., 2006. Impact constraints on, and a chronology for, major events in early Mars history. J. Geophys. Res. 111, E08S91.
Gazel, E., McSween, H.Y., Moore, L.R., 2016. Crustal Evolution of Earth and Mars. In: 47th Lunar and Planetary Science Conference. LPI Contribution No. 1903, p. 1619.
Golombek, M.P., Bridges, N.T., 2000. Erosion rates on Mars and implications for climate change: constraints from the Pathfinder landing site. J. Geophys. Res. 105 (E1), 1841–1853. doi:10.1029/1999JE001043.
Grott, M., Breuer, D., 2009. Implications of large elastic thicknesses for the composition and current thermal state of Mars. Icarus 201 (2), 540–548.
Grott, M., Breuer, D., 2010. On the spatial variability of the martian elastic lithosphere thickness: evidence for mantle plumes? J. Geophys. Res. 115, E03005. doi:10.1029/2009JE003456.
Grott, M., Hauber, E., Werner, S.C., Kronberg, P., Neukum, G., 2007. Mechanical modeling of thrust faults in the Thaumasia region, Mars, and implications for the Noachian heat flux. Icarus 186, 517–526.
Hahn, B.C., McLennan, S.M., Klein, E.C., 2011. Martian surface heat production and crustal heat flow from Mars Odyssey Gamma Ray Spectrometry. Geophys. Res. Lett. 38, L14203. http://dx.doi.org/10.1029/2011GL047435.
Hartmann, W.K., 2005. Martian cratering 8. Isochron refinement and the history of Martian geologic activity. Icarus 174, 294–320.
Hauck, S.A., et al., 2004. Internal and tectonic evolution of Mercury. Earth Planet. Sci. Lett. 222, 713–728.
Hauck, S.A., Phillips, R.J., 2002. Thermal and crustal evolution of Mars. J. Geophys. Res. 107, 5052. doi:10.1029/2001JE001801.
Head, J.W., Murchie, S.L., Prockter, L.M., et al., 2008. Volcanism on Mercury: Evidence from the first MESSENGER flyby. Science 321 (5885), 69–72.
Ivanov, B.A., Neukum, G., Wagner, R., 2001. Size-frequency distributions of planetary impact craters and asteroids. In: Marov, M.Y., Rickman, H. (Eds.). In: Astrophysics and Space Science Library, 261. Astrophysics and Space Science Library, pp. 1–34.
Kieffer, H.H., et al., 1977. Thermal and albedo mapping of Mars during the Viking primary mission. J. Geophys. Res. 82, 4249–4291.
King, G.C.P., Stein, R.S., Rundle, J.B., 1988. The growth of geological structures by repeated earthquakes 1, Conceptual framework. J. Geophys. Res. 93 (13), 307–313 318.
Klimczak, C., Watters, T.R., Ernst, C.M., et al., 2012. Deformation associated with ghost craters and basins in volcanic smooth plains on Mercury: Strain analysis and implications for plains evolution. J. Geophys. Res. 117 (E12).
Klimczak, C., 2014. Geomorphology of lunar grabens requires igneous dikes at depth. Geology 42 (11), 963–966.
Kneissl, T., Michael, G.G., Platz, T., Walter, S.H.G., 2015. Age determination of linear surface features using the Buffered Crater Counting approach—Case studies of the Sirenum and Fortuna Fossae graben systems on Mars. Icarus 250, 384–394.
Kneissl, T., van Gasselt, S., Neukum, G., 2011. Map-projection-independent crater size-frequency determination in GIS environments—New software tool for ArcGIS. Planet. Space Sci. 59, 1243–1254.
Koch, P.S., Christie, J.M., Ord, A., George, R.P., 1989. Effect of water on the rheology of experimentally deformed quartzite. J. Geophys. Res. 94 13,966–13,975.
Konopliv, A.S., et al., 2011. Mars high resolution gravity fields from MRO, Mars seasonal gravity, and other dynamical parameters. Icarus 211 (1), 401–428.
Leonard, G.J., Tanaka, K.L.. Geologic map of the Hellas region of Mars: U.S. Geological Survey Geologic Investigations Series I–2694 pamphlet 10 p., 1 plate, scale 1:4,336,000, available at.
Lin, J., Stein, R.S., 2004. Stress triggering in thrust and subduction earthquakes, and stress interaction between the southern San Andreas and nearby thrust and strike-slip faults. J. Geophys. Res. 109, B02303. doi:10.1029/2003JB002607.
McGovern, P.J., et al., 2002. Localized gravity/topography admittance and correlation spectra on Mars: implications for regional and global evolution. J. Geophys. Res. 107, 5136. doi:10.1029/2002JE001854.
McGovern, P.J., et al., 2004. Correction to localized gravity/topography admittance and correlation spectra on Mars: implications for regional and global evolution. J. Geophys. Res. 109, E07007. doi:10.1029/2004JE002286.
Meyer, C., 2003. Mars Meteorite Compendium. Lyndon B. Johnson Space Cent., NASA, Houston, Tex.
Michael, G.G., Neukum, G., 2010. Planetary surface dating from crater size–frequency distribution measurements: partial resurfacing events and statistical age uncertainty. Earth Planet. Sci. Lett. 294, 223–229.
Moser, D.E., Chamberlain, K.R., Tait, K.T., Schmitt, A.K., Darling, J.R., Barker, I.R., Hyde, B.C., 2013. Solving the Martian meteorite age conundrum using micro-baddeleyite and launch-generated zircon. Nature 499 (7459), 454–457.
Mueller, K., Vida, A., Robbins, S., Golombek, M., West, C., 2014. Fault and fold growth of the Amenthes uplift: implications for Late Noachian crustal rheology and heat flow on Mars. Earth Planet. Sci. Lett. 408, 100–109.
Nahm, A.L., Schultz, R.A., 2011. Magnitude of global contraction on Mars from analysis of surface faults: Implications for martian thermal history. Icarus 211, 389–400.
Nahm, A., Peterson, S., 2016, March. Automated Forward Mechanical Modeling of Wrinkle Ridges on Mars. In: Lunar and Planetary Science Conference, Vol. 47, p. 1186.
Neumann, G.A., et al., 2004. The crustal structure of Mars from gravity and topography. J. Geophys. Res. 109, E08002. doi:10.1029/2004JE002262.
Neumann, G.A., Lemoine, F.G., Smith, D.E., Zuber, M.T., 2008. Marscrust3-A crustal thickness inversion from recent MRO gravity solutions. In: Proc. Lunar Planet. Sci. Conf., 39 Abstract 2167.
Nyquist, L.E., Bogard, D.D., Shih, C.-Y., Greshake, A., Stoffler, D., Eugster, O., 2001. Age and geologic histories of Martian meteorites. Space Sci. Rev. 96, 105–164.
Nyquist, L.E., Borg, L.E., Shih, C.-Y., 1998. The Shergottite age paradox and the relative probabilities for Martian meteorites of differing ages. J. Geophys. Res. 103 31,445–31,455.
Öhman, T., Aittola, M., Kostama, V.P., Raitala, J., 2005. The preliminary analysis of polygonal impact craters within greater Hellas region, Mars. In: Impact Tectonics. Springer, Berlin Heidelberg, pp. 131–160.
Okada, Y., 1992. Internal deformation due to shear and tensile faults in a half-space. Bull. Seismol. Soc. Am. 82 (2), 1018–1040.
Phillips, R.J., et al., 2008. Mars north polar deposits: stratigraphy, age, and geodynamical response. Science 320 (5880), 1182–1185.
Ranalli, G., 1997. Rheology of the lithosphere in space and time. Geol. Soc. Spec. Pub. 121, 19–37.
Ritzer, J.A., Hauck, S.A., Barnouin, O.S., et al., 2010. Mechanical Structure of Mercury's Lithosphere from MESSENGER Observations of Lobate Scarps. Lunar Planet. Sci. Conf. 41st., 2122 Abstract 1533.
Robbins, S.J., Hynek, B.M., 2012. A new global database of Mars impact craters ≥1 km: 1. Database creaton, properties, and perameters. J. Geophys. Res. 117, E05004. doi:10.1029/2011JE003966.
Roberts, J.H., Lillis, R.J., Manga, M., 2009. Giant impacts on early Mars and the cessation of the Martian dynamo. J. Geophys. Res. 114, E04009. doi:10.1029/2008JE003287.
Rogers, A.D., Nekvasil, H., 2015. Feldspathic rocks on Mars: compositional constraints from infrared spectroscopy and possible formation mechanisms. Geophys. Res. Lett. 42, 2619–2626.
Ruedas, T., Tackley, P.J., Solomon, S.C., 2013. Thermal and compositional evolution of the martian mantle: effects of phase transitions and melting. Phys. Earth Planet. Inter. 216, 32–58.
Ruiz, J., et al., 2008. Ancient heat flow, crustal thickness, and lithospheric mantle rheology in the Amenthes region. Mars. Earth Planet. Sci. Lett. 270, 1–12.
Ruiz, J., et al., 2011. The thermal evolution of Mars as constrained by paleo-heat flows. Icarus 215, 508–517.
Ruiz, J., 2014. The Early Heat Loss Evolution of Mars and Their Implications for Internal and Environmental History, p. 4338, Scientific Reports 4. doi:10.1038/srep04338.
Ruiz, J., Williams, J.P., Dohm, J.M., Fernández, C., López, V., 2009. Ancient heat flows and crustal thickness at Warrego rise, Thaumasia Highlands, Mars: implications for a stratified crust. Icarus 207, 631–637.
Sautter, V., et al., 2015. In situ evidence for continental crust on early Mars. Nat. Geosci. 8, 605–609.
Sautter, V., Toplis, M.J., Beck, P., et al., 2016. Magmatic complexity on early Mars as seen through a combination of orbital, in-situ and meteorite data. Lithos 254, 36–52.
Schultz, R.A., 2003. Seismotectonics of the Amenthes Rupes thrust fault population, Mars. Geophys. Res. Lett. 30, 1303. doi:10.1029/2002GL016475.
Schultz, R.A., Watters, T.R., 2001. Forward mechanical modeling of the Amenthes Rupes thrust fault on Mars. Geophys. Res. Lett. 28, 4659–4662.
Smith, D.E., et al., 1999. The global topography of Mars and implications for surface evolution. Science 284, 1495–1503. doi:10.1126/science.284.5419.1495.
Taboada, A., Bousquet, J.C., Philip, H., 1993. Coseismic elastic models of folds above blind thrusts in the Betic Cordilleras (Spain) and evaluation of seismic hazard. Tectonophysics 220, 223–241.
Tanaka, K.L., 1982. A new time-saving crater-count technique, with application to narrow features. In: NASA Technical Memo. NASA, pp. 123–125. TM-85127.
Tanaka, K.L., et al., 2014. The digital global geologic map of Mars: Chronostratigraphic ages, topographic and crater morphologic characteristics, and updated resurfacing history. Planet. Space Sci. 95, 11–24. doi:10.1016/j.pss.2013.03.006.
Taylor, G.J., Boynton, W., Brückner, J., et al., 2006. Bulk composition and early differentiation of Mars. J. Geophys. Res. 111, E03S10.
Toda, S., Stein, R.S., Richards-Dinger, K., Bozkurt, S., 2005. Forecasting the evolution of seismicity in southern California: animations built on earthquake stress transfer. J. Geophys. Res. 110, B05S16. doi:10.1029/2004JB003415.

Watters, T.R., Robinson, M.S., 1999. Lobate scarps and the Martian crustal dichotomy. J. Geophys. Res. 104, 18981–18990. doi:10.1029/1998JE001007.
Watters, T.R., Schultz, R.A., Robinson, M.S., Cook, A.C., 2002. The mechanical and thermal structure of Mercury's early lithosphere. Geophys. Res. Lett. 29. doi:10.1029/2001GL014308, 37-1.
Watters, T.R., Schultz, R.A., 2010. Planetary Tectonics. Cambridge University Press.
Watters, W.A., Zuber, M.T., Hager, B.H., 2009. Thermal perturbations caused by large impacts and consequences for mantle convection. J. Geophys. Res. 114 (E2).
Watts, A.B., 2001. Isostasy and Flexure of the Lithosphere. Cambridge University Press, p. 472.
Wessel, P., et al., 2013. Generic mapping tools: improved version released. EOS Trans. AGU 94, 409–410.
Wichman, R.W., Schultz, P.H., 1989. Sequence and mechanisms of deformation around the Hellas and Isidis impact basins on Mars. J. Geophys. Res. 94, 17333–17357.
Wieczorek, M.A, Meschede, M., Oshchepkov, I., 2016. SHTOOLS: Version 3.2. Zenodo. doi:10.5281/zenodo.55790.
Wieczorek, M.A., 2015. Gravity and topography of the terrestrial planets. In: Schubert, G. (Ed.), Treatise On Geophysics 2nd ed. Elsevier, Oxford, pp. 153–193.
Wieczorek, M.A., Phillips, R.J., 1998. Potential anomalies on a sphere: applications to the thickness of the lunar crust. J. Geophys. Res. 103, 1715–1724.
Wieczorek, M.A., Zuber, M.T., 2004. Thickness of the martian crust: improved constraints from geoid-to-topography ratios. J. Geophys. Res. 109, E01009. doi:10.1029/2003JE002153.
Williams, J.-P., Nimmo, F., 2004. Thermal evolution of the martian core: Implications for an early dynamo. Geology 32, 97–100.
Wray, J.J., et al., 2013. Prolonged magmatic activity on Mars inferred from the detection of felsic rocks. Nat. Geosci. 6, 1013–1017.
Yoder, C.F., Konopliv, A.S., Yuan, D.N., Standish, E.M., Folkner, W.M., 2003. Fluid core size of Mars from detection of the solar core. Science 300, 299–303.
Zuber, M.T., et al., 2000. Internal structure and early thermal evolution of Mars from Mars global surveyor. Science 287, 1788–1793.